Advanced Healthcare Materials

ADVANCED HEALTHCARE MATERIALS
www.advhealthmat.de

RESEARCH ARTICLE

4D-Printed Intelligent Reconfigurable Occluder With Anti-Thrombotic and Rapid-Repairing Capabilities for Patent Foramen Ovale

Jingfei Wang[1] | Shuting Li[3] | Liwu Liu[1] | Fukai Liu[3] | Cheng Lin[2] | Yanju Liu[1,4] | Jinsong Leng[2]

[1]Department of Astronautical Science and Mechanics, Harbin Institute of Technology, Harbin, China | [2]Centre For Composite Materials and Structures, Harbin Institute of Technology, Harbin, China | [3]Animal Laboratory Center, The First Affiliated Hospital of Harbin Medical University, Harbin, China | [4]Suzhou Research Institute, Harbin Institute of Technology, Suzhou, China

Correspondence: Fukai Liu (liufukai@hrbmu.edu.cn) | Cheng Lin (lincheng@hit.edu.cn) | Yanju Liu (yj_liu@hit.edu.cn)

Received: 13 November 2025 | **Revised:** 25 January 2026 | **Accepted:** 25 January 2026

Keywords: 4D printing | shape memory | patent foramen ovale | bioabsorbable occluder | endothelialization | anti-thrombotic

ABSTRACT

Nowadays, the implantation of occluder is an effective approach for treating patent foramen ovale (PFO); however, the slow endothelialization poses significant complications associated with occlusion devices. Herein, a 4D-printed intelligent reconfigurable PFO occluder with pro-endothelialization, anti-thrombosis, and absorbability is designed. The combination of the occluder implantation and topical drug delivery of anti-thrombosis drugs offers a solution to stroke. The occluder is designed based on the biomimetic structure, facilitating the integration of mechanical response behavior compatible with cardiac tissue. In vitro degradation and in vivo histological examination demonstrate the bioabsorbability of the occluder, and the anti-thrombosis efficacy is preliminarily demonstrated through anti-thrombosis experiments. The effective expression of VWF and CD31 markers validates the superior pro-endothelial efficacy of the occluder. To summarize, the 4D-printed occluder in this work represents an accessible strategy to combat PFO through integrated occlusion and topical drug delivery.

1 | Introduction

The foramen ovale is a weak area located between the left and right atria, through which venous blood passes directly into the left atrium during the embryonic period. Physiological closure typically occurs postnatally through the establishment of pulmonary circulation and an increase in left atrial pressure. Failure of this natural closure process results in patent foramen ovale (PFO), a highly prevalent congenital cardiac malformation constituting approximately 25 % of congenital heart defects. PFO is closely associated with a variety of serious, life-threatening clinical diseases, including myocardial infarction and stroke [1–3].

The traditional treatment of PFO is oral anticoagulant drugs, but increasing studies have shown that implanting an occluder to close PFO has significant advantages in preventing stroke and migraine [4]. The implantation of the PFO occluder will lead to the initiation of the endothelialization process, manifested as the adhesion and proliferation of surrounding tissues and the final coating. However, the widely used occluders are made of non-degradable alloy, and the permanent retention of alloy may lead to problems such as metal ion allergy, structural erosion, and displacement thrombosis [5, 6]. More notably, in essence, the slow rate of endothelialization is a core factor that leads to various complications of the occluder, which is often underestimated in clinical importance. Therefore, there is an urgent need to develop a PFO occluder that is highly effective in accelerating endothelialization, anti-thrombosis, and bio-absorbability, thus providing effective solutions for various complications [7–10].

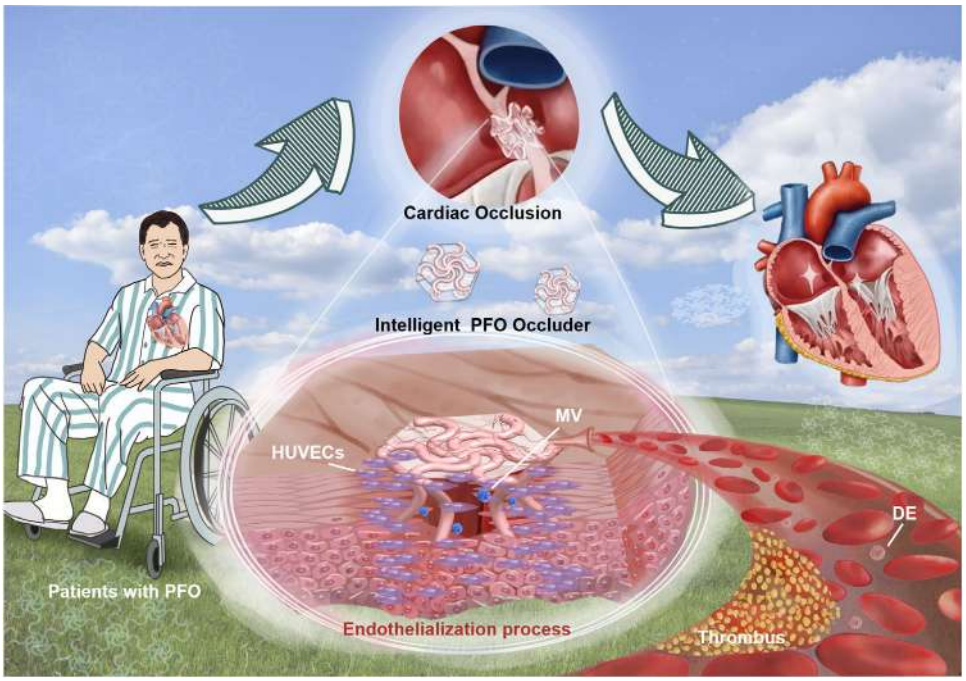

FIGURE 1 | Schematic diagram of the 4D-printed intelligent reconfigurable PFO occluder (DE: dabigatran etexilate, MV: mevastatin, PFO: patent foramen ovale, HUVECs: human umbilical vein endothelial cells).

In this work, we developed an anti-thrombotic, pro-endothelial, bioabsorbable, customizable, and 4D-printed intelligent reconfigurable PFO occluder, consisting of a multifunctional drug-loaded occlusion layer and a 4D-printed shape memory framework (Figure 1). The 4D-printed shape memory framework can achieve minimally invasive implantation through shape memory-driven structure reconstruction [11]. A series of biomimetic microstructure networks was designed to achieve J-shaped stress–strain behavior, emulating the distinctive mechanical performance observed in biological tissues [12, 13]. The multifunctional drug-loaded occlusion layer was equipped with the antithrombosis drug dabigatran etexilate (DE) and the endothelialization drug mevastatin (MV) to achieve topical drug delivery of antithrombosis drugs [14–16]. The bioabsorbability and anti-thrombosis effects of the occluder were evaluated through in vitro and in vivo degradation studies and coagulation factor inhibition analysis. The pro-endothelial effect was validated by examining the micromorphology of adjacent tissues and assessing the expression levels of endothelial cell markers VWF and CD31 following implantation. To sum up, this work opened up an avenue for synergistic stroke treatment by developing a multifunctional intelligent PFO occluder that combined PFO occlusion with targeted anti-thrombosis drugs.

2 | Results and Discussion

2.1 | Preparation and Characterization of the Multifunctional Drug-Loaded Occlusion Layer

The occlusion layer of the existing occluder is primarily composed of simple polymer membranes, such as polyethylene (PE), polycaprolactone (PCL), and polylactic acid (PLA), which only provide physical occlusion and lack functional properties [17, 18]. To address this limitation, a multifunctional drug-loaded occlusion layer with anti-thrombosis drug DE and endothelialization drug MV was designed (DE-MV/gPLA) (Figure 2A). As shown in the Fourier Transform Spectroscopy (FTIR) spectra in Figure 2B, it can be observed that the C—COO stretching at 960 cm^{-1} and the COC symmetric stretching at 1090 cm^{-1}, which were the characteristic peaks of PLA and polyethylene glycol (PEG), respectively. There was also a CH_2 symmetric stretching at 2882 cm^{-1}, which was associated with PEG. The characteristic peaks observed at 1752 cm^{-1} can be attributed to C═O telescopic vibrations, possibly related to DE. As the drug concentration increased, the peak intensity of 1752 cm^{-1} showed an upward trend.

The biodegradability of DE-MV/gPLA constituted a defining feature, so in vitro degradation experiments were needed to simulate the performance evolutions of DE-MV/gPLA after implantation. The morphology analysis showed that micro-pores appeared on the surface of DE-MV/gPLA after degradation for 14 days (Figure S2). Over time, the diameter of the micro-pores, the number of micro-pores, and the weight loss rate all increased. Micropores were generated by the degradation of the polymer matrix to produce oligomers and monomers, which escaped from the polymer surface when the degradation products accumulated to a certain extent [19]. In addition, weight decreased as degradation time increased, while 3 % DE-MV/gPLA exhibited the highest rate of degradation weight loss ratio (Figure 2C). The FTIR spectrum showed that the C—COO stretching at 964 cm^{-1} and the —CH_2 symmetric stretching at 2909 cm^{-1} decreased with the prolonged degradation time, which was attributed to the hydrolysis of PLA (Figure 2D) [20, 21]. The high-resolution X-ray photoelectron spectroscopy (XPS) further verified the relationship between the material properties of DE-MV/gPLA and the concentration and degradation time. The presence of N element in the survey

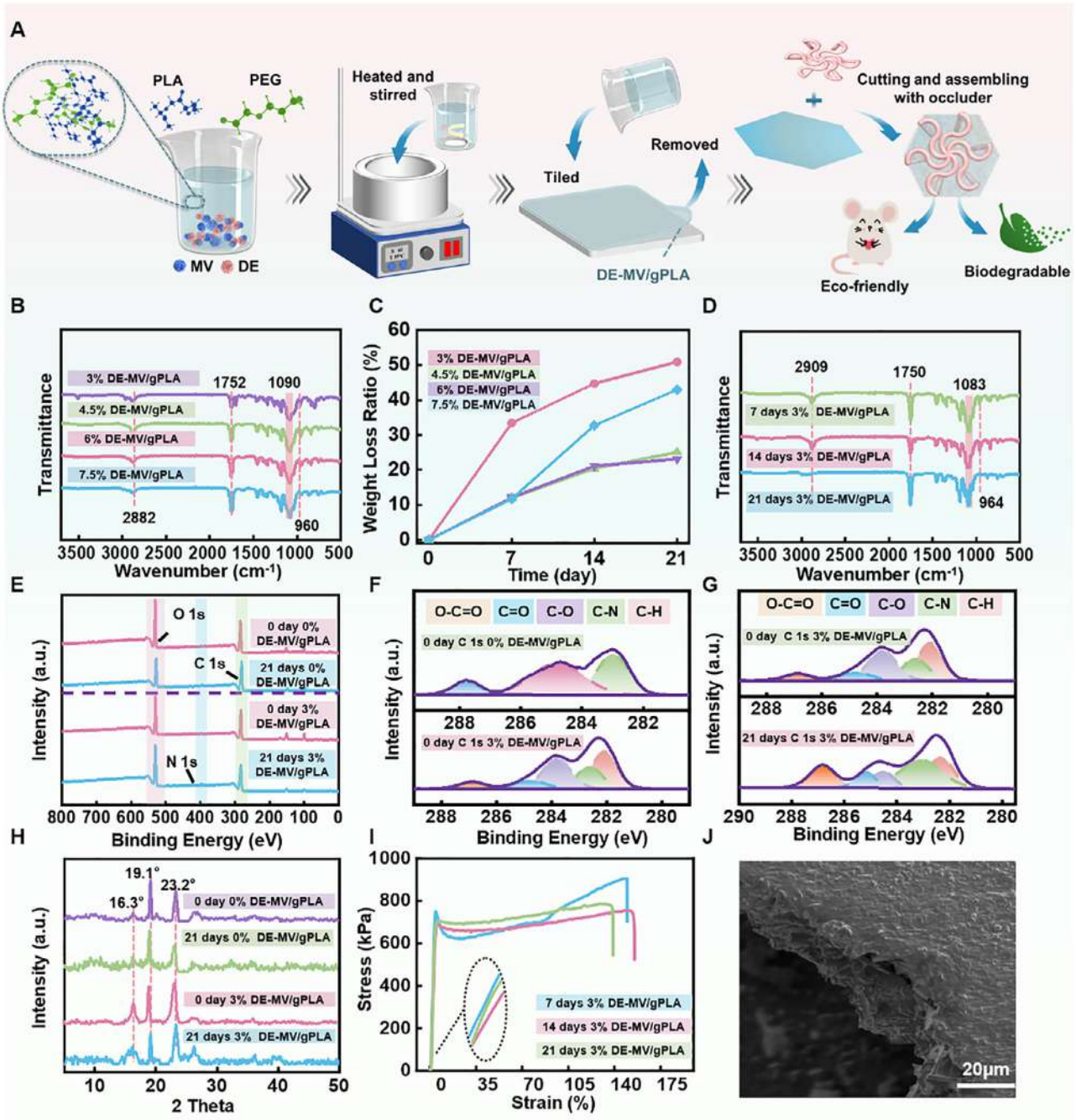

FIGURE 2 | Preparation and characterization of the multifunctional drug-loaded occlusion layer. (A) Preparation of the DE-MV/gPLA. (B) FTIR curves of DE-MV/gPLA at different drug concentrations. (C) Weight loss ratio of DE-MV/gPLA at different drug concentrations. (D) FTIR curves of DE-MV/gPLA at different degradation times. (E) The XPS survey spectrum of DE-MV/gPLA. (F) C1s XPS spectra at different drug concentrations. (G) C1s XPS spectra at different degradation times. (H) XRD curves of DE-MV/gPLA at different degradation times. (I) Stress–strain curves of DE-MV/gPLA at different degradation times. (J) SEM image of the vertical fracture of the DE-MV/gPLA tensile specimen.

spectra of 3 % DE-MV/gPLA further demonstrated the successful loading of the drugs, and the significant decrease in the peak of O element after degradation also demonstrated the hydrolysis progress (Figure 2E). In addition, C—N and O—C═O in 3 % DE-MV/gPLA were the characteristic chemical bonds associated with DE and MV (Figure 2F). The C1s spectrum post-degradation showed a significant reduction in the intensity of C—O and C—H peaks, indicating the hydrolysis of DE-MV/gPLA, consistent with FTIR characterization (Figure 2G). Additionally, the effect of degradation on the crystallization properties of DE-MV/gPLA was analyzed through X-ray Diffraction (XRD) (Figure 2H). The (200) and (203) reflections of the α crystal phase in PLA were observed at 2θ = 16.3° and 19.1°, respectively. Compared with 0 % DE-MV/gPLA, the diffraction peak of 3 % DE-MV/gPLA was significantly stronger at 16.3°, which may be due to the interaction between DE and MV and matrix PLA-PEG during the preparation process, which improved the crystallinity of PLA. Compared with the XRD spectra of 21 days of degradation, the

peak decreased to a certain extent at 16.3° and 19.1°, which was related to the hydrolysis of the PLA. The thermal properties of DE-MV/gPLA were analyzed through differential scanning calorimetry (DSC) (Figure S7). As drug concentration increased, both the melting temperature and glass transition temperature peaks shifted toward higher temperatures, which may result from melt recrystallization during heating.

In addition, the effects of drug concentration and degradation time on the mechanical properties of DE-MV/gPLA were discussed. The tensile strength of 3 % DE-MV/gPLA was 744.9 kPa after degradation for 7 days, and decreased to about 703.3 kPa after degradation for 21 days (Figure 2I). But with the extension of degradation time, the tensile strength did not fluctuate significantly in the range of 700–800 kPa. The elongation at break decreased slightly after degradation, but it was still as high as about 138.9 % after 21 days of degradation. The excellent strength and toughness of DE-MV/gPLA provided favorable support for the effective occlusion of the multifunctional drug-loaded occlusion layer of the 4D-printed intelligent reconfigurable PFO occluder. Microscopic morphology of the DE-MV/gPLA tensile specimens was observed through a scanning electron microscope (SEM). The vertical fracture surface showed irregular morphological features (Figures 2J; S8 and S9), which contrasted sharply with the smooth fracture morphology of the pure PLA matrix and were in accordance with the significantly increased elongation at break of DE-MV/gPLA [22]. Additionally, FTIR and XRD analyses (Figure 2D,H) revealed no significant changes in characteristic drug peaks (1752 cm^{-1} and $2\theta = 16.3°$) during degradation. This confirmed the structural and compositional integrity of the drug throughout the gradual degradation of the occluder and sustained drug release process.

2.2 | Design and Characterization of the Biomimetic Microstructure Networks

Collagen fibril-inspired wave microstructures possess a distinctive advantage in design flexibility, enabling the demonstration of J-shaped stress–strain curves that are compatible with the mechanical responses of biological tissues (Figure 3A) [23–25]. Therefore, the biomimetic microstructure was designed with the goal of achieving J-shaped mechanical behavior similar to that of biological tissues, and was used as the structural basis of the intelligent PFO occluder to achieve collaborative tissue deformation and reduce wear. To establish the relationship between key geometric design variables and the mechanical response of biomimetic structures, eight networks were devised by regulating the node configuration, ligament configuration, and the number of ligaments, including rounded ligament networks with different node configurations and with different combined ligament configurations (Figure 3B; Table S1). The wave-shaped biomimetic microstructure networks were obtained by arraying the wave-shaped biomimetic microstructure cells, and were fabricated using 4D printing technology, which can achieve shape recovery at a temperature slightly higher than body temperature (Figures 3C; S11).

The mechanical properties of the biomimetic microstructure networks were analyzed. As depicted in Figure 4A, the node configurations of RLN1, RLN2, RLN3, and RLN4 were hollow circles, solid circles, hollow square and solid squares, respectively. RLN3 and RLN4 exhibited higher maximum elastic moduli than RLN1 and RLN2, respectively, indicating that the mechanical properties of the networks comprised of square nodes were superior to those formed by circular nodes. Compared with square nodes, the RLN2 with circular nodes had a better toughness. RLN2 exhibited excellent tensile properties, achieving a tensile strength of 424.8 kPa at an elongation exceeding 78 %. Notably, characteristic points on the stress–strain curve suggested the onset of localized microstructural damage within the biomimetic microstructure network prior to final rupture. On the whole, the modulus of CLN5-CLN8 was significantly better than that of RLN1-RLN4. This might be because CLN5-CLN8 had more ligaments (Figure 4B). CLN5 exhibited the highest tensile strength, possibly because of more ligamentous junctions and higher surface coverage. Compared with CLN5, CLN6, and CLN7, CLN8 exhibited significantly superior mechanical properties and a tensile strength greater than 960 kPa, which may be due to its more compact structure design and higher curvature of its combined ligaments. Among various structures, RLN2, CLN5, and CLN8 exhibited the optimal mechanical properties and were selected for subsequent analysis. Figure 4C exhibited the weight loss ratio curves of RLN2, CLN5, and CLN8. After 21 days of degradation, the weight loss ratios of RLN2, CLN5, and CLN8 were about 28.9 %, 10.6 %, and 11.4 %, which verified the degradability of the biomimetic microstructure networks. The experimental testing and finite element analysis were employed to analyze the deformation process of the biomimetic networks, and the results showed excellent consistency. As evidenced by the comparative analysis between simulation and experimental results, a consistent deformation pattern was observed (Figure 4D). The deformation process is initiated with the progressive straightening of the initially curved ligaments, subsequently transitioning into the stage dominated by tensile deformation. The cyclic performance of the biomimetic microstructure networks was analyzed to explore their post-implantation stability, and the results showed that they still had outstanding cyclic stability and durability after 500 cycles (Figure 4E–J). RLN2, CLN5, and CLN8 exhibited similar cyclic behaviors. In the stretching cycle, it can be seen that the unloading curve lagged behind the loading curve, indicating that there was residual strain in each cycle, and a certain energy loss was generated, but the network did not fail after 500 cycles, indicating that it had good durability [26].

2.3 | Preparation and Characterization of the 4D-Printed Intelligent Reconfigurable PFO Occluder

2.3.1 | Mechanical Performance

Based on the biomimetic microstructure, the 4D-printed shape memory framework was designed and fabricated (Figure 5A), and the number of lumbar ligaments was set according to the cell structures, including the rounded ligament occluder and the combined ligament occluder. The 4D-printed shape memory framework was combined with the DE-MV/gPLA at different drug concentrations to prepare the 4D-printed intelligent reconfigurable PFO occluder. Mechanical experiments were carried out on the eight kinds of intelligent PFO occluders to test their structural properties. Figure 5B showed an illustration of the intelligent PFO occluder compression and compression

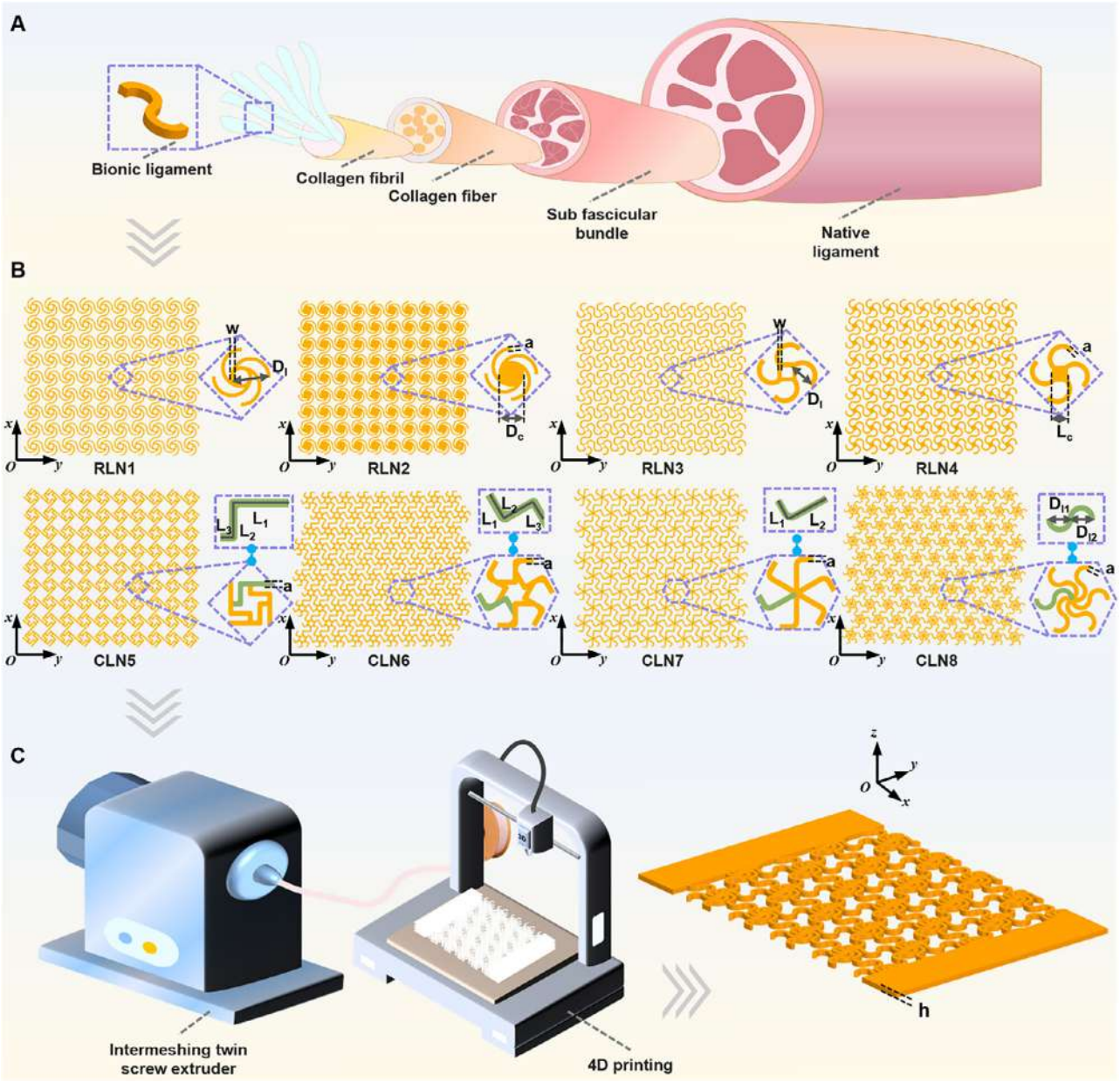

FIGURE 3 | Schematic diagram of the design and preparation process of the biomimetic microstructure networks. (A) Schematic diagram of collagen fibril-inspired design. (B) Design parameters of the biomimetic networks. (C) Preparation of the biomimetic networks.

cycle experiment. During the compression process, the height of the intelligent PFO occluder under compression load gradually decreased. The stress–strain curve of the intelligent PFO occluder was mainly divided into three stages: the linear stage, the serrated stage, and the ascending stage (Figure 5C,D). The waist of the intelligent PFO occluder served as the load-bearing component. As the compression proceeded, the distance between the two discs reduced, resulting in a gradual increase in strain and an approximately linear upward trend in stress. Then, a sawtooth fluctuation stage followed, which was caused by local failure of the waist due to load bearing. After the sawtooth stage, the waist completely failed, and the upper and lower surfaces of the intelligent PFO occluder came into contact, causing the modulus to rapidly increase. The carrying capacity of RLO2 was better than that of RLO1, RLO3, and RLO4. CLO5, CLO6, CLO7, and CLO8 had similar compressive stress–strain behavior, with maximum strains ranging from 127.7 % to 147.7 %. The maximum strain of CLO5 was lower than that of CLO6, CLO7, and CLO8, but the equivalent stiffness was the largest, which may be due to its relatively closed structural design, thus enabling it to withstand compressive loads more effectively.

In order to analyze the performance evolution of the intelligent PFO occluder after implantation, in vitro degradation was conducted to evaluate the correlation between degradation progress and mechanical property evolution. With the progress of degradation, the weight loss ratio gradually increased (Figure 5E). After 21 days, the weight loss rates of CLO2, CLO5, and CLO8 were 25.9 %, 20.2 %, and 14.4 %, respectively, which once again proved the degradable properties. Figure 5F–H showed the stress–strain curves of the intelligent PFO occluder after degradation. The compression modulus showed an overall decreasing trend after

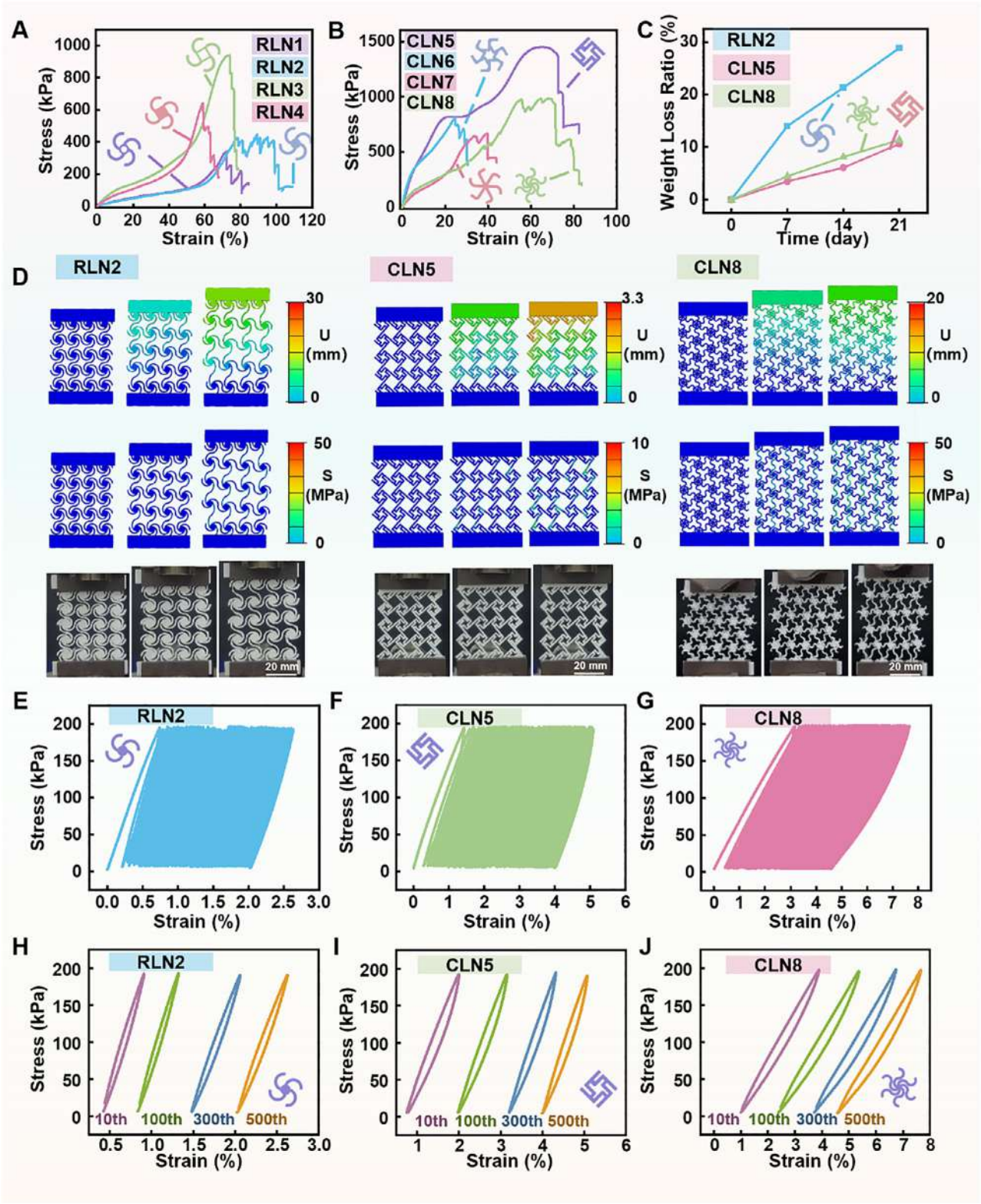

FIGURE 4 | Characterization of the biomimetic microstructure networks. (A,B) Tensile curves of the biomimetic microstructure networks. (C) The weight loss ratio of RLN2, CLN5 and CLN8. (D) The deformation process of RLN2, CLN5, and CLN8 was analyzed by finite element methods and experimentally. (E–G) The tensile cyclic curves of RLN2, CLN5, and CLN8. (H–J) The 10th, 100th, 300th and 500th cyclic curves of RLN2, CLN5 and CLN8.

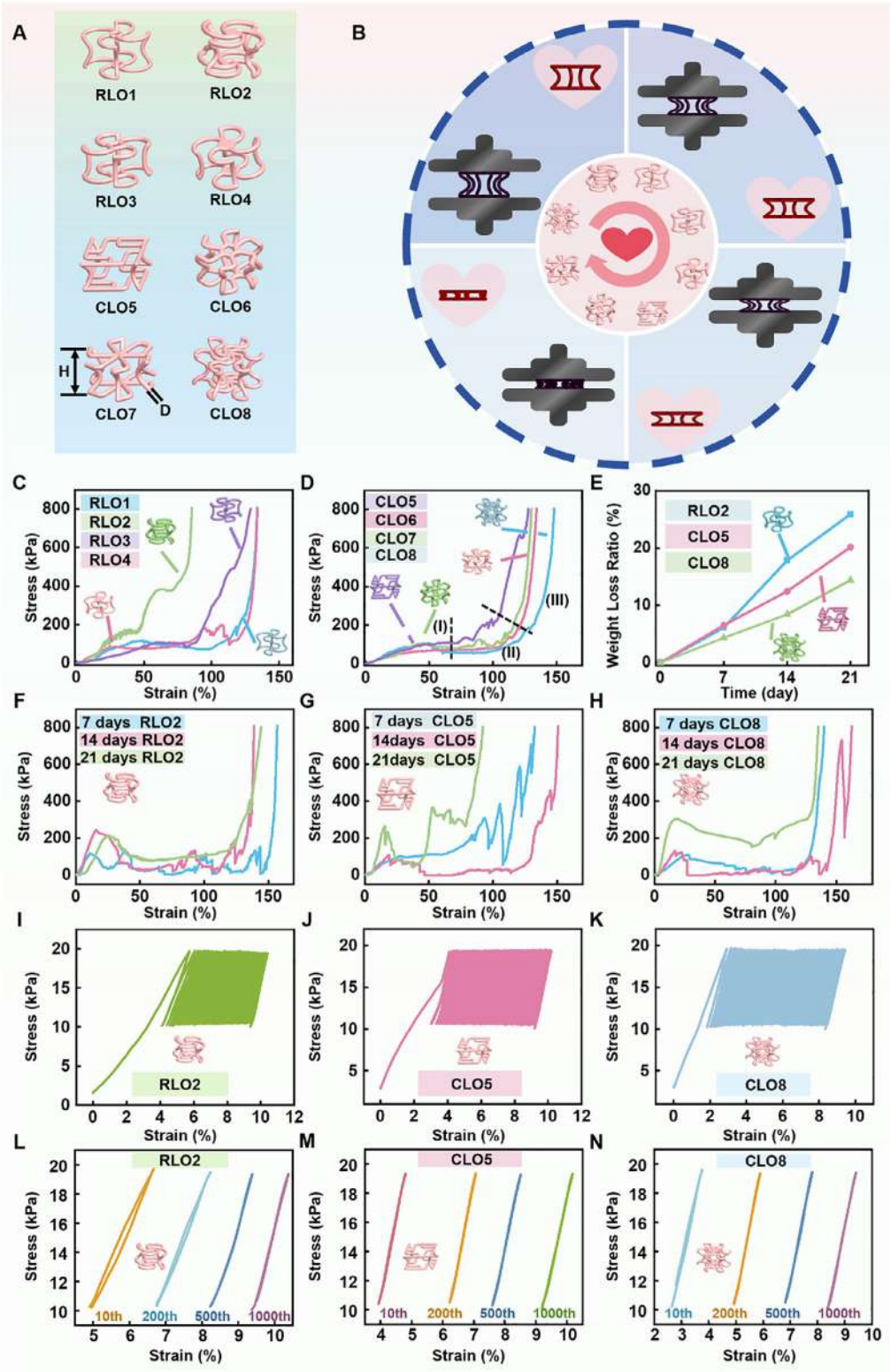

FIGURE 5 | Characterization of the 4D-printed intelligent reconfigurable PFO occluder. (A) Schematic diagram of the intelligent PFO occluder. (B) Schematic diagram of the intelligent PFO occluder experiencing compression and cyclic compression. (C,D) The compression curve of the intelligent PFO occluder. (E) The weight loss ratio of the intelligent PFO occluder. (F–H) The compression properties of RLO2, CLO5, and CLO8 degraded at different times. (I–K) The compression behavior of RLO2, CLO5, and CLO8. L-N) The 10th, 200th, 500th, and 1000th compression cycles of RLO2, CLO5, and CLO8.

degradation, and the sawtooth fluctuation increased significantly. The post-degradation photograph of the occluder demonstrated the absence of macroscopic structural defects, confirming structural continuity after degradation (Figure S19). In addition, 1000 compression cycles were performed to analyze the stability of the intelligent PFO occluder (Figure 5I–K). Remarkably, the intelligent PFO occluder maintained its structural integrity after enduring up to 1000 cycles, preliminarily demonstrating its ability to serve effectively in the body for a long time. Representative single-cycle curves from the 10th, 200th, 500th, and 1000th cycles (Figure 5L–N) were selected to comprehensively elucidate the characteristic features of each stage. It was evident that the single-cycle curves for RLO2, CLO5, and CLO8 across different stages exhibited a minimal hysteresis area, suggesting that energy loss per cycle was relatively low.

2.3.2 | Reconfigurable Shape Memory Performance and Occlusion Effect

CLO8 was selected as the final structure for the preparation of the occluder. By combining CLO8 with 0 % DE-MV/gPLA, 3 % DE-MV/gPLA, and 4.5 % DE-MV/gPLA, the 4D printed intelligent reconfiguration occluder with anti-thrombosis and endothelialization effect was obtained (named 0 %CLO8, 3 %CLO8, and 4.5 %CLO8). Taking 0 % CLO8 as a representative case, the reconfigurable shape memory behavior of the reconfiguration occluder was analyzed (Figure 6A). In order to better characterize the shape memory performance, the area to be calibrated was selected first.

The 0 % CLO8 was programmed into a temporary shape of a small volume, and its shape recovery ability was assessed under thermal stimulation (Figure S21). D_1, D_2, and D_3 represented the disc areas at distinct stages of shape recovery (Table S2). In comparison to the undeformed shape, the disc area of the temporary shape was reduced to 65.9 % of the initial shape. 0 % CLO8 underwent shape recovery during the reconfigurable deformation, with the disc area of the reverted shape recovering to 95.3 % of its initial shape within 20 s. The intelligent PFO occluder exhibited shape-memory properties, enabling successful reconfigurable deployment at the defect site and achieving effective occlusion.

Cyclic shape-memory testing across 10 iterations revealed no substantial decline in recovery rate (cycle 10:96.2 % of the disk while cycle 1:97.9 % of the disk, Figure S22 and Table S3). Given that clinical application necessitates just one transformation, this durability suffices for practical requirements.

2.3.3 | Biocompatible and Pro-Endothelial Performance

In vivo characterization was conducted to assess the biocompatibility of the intelligent PFO occluder, a critical determinant for its clinical functionality. The intelligent PFO occluder was implanted and can be clearly observed under X-rays (Figures 6B; S23) due to the presence of barium sulfate, which was of vital importance for precise positioning during the surgical procedure and effectively averted the issue of inaccurate positioning resulting from the current few developer points for visualization. The peripheral tissues and major organs of rats were collected for histological analysis. Figure 6C shows the physical diagram of the intelligent PFO occluder implanted subcutaneously at different times. After implantation, the tissue gradually adhered to the intelligent PFO occluder, and by 14 days post-implantation, the tissue had fully covered the disc surface. Compared with 0 % CLO8, the tissue covered by 3 % CLO8 and 4.5 % CLO8 on the disc surface was significantly increased, which proved the pro-endothelial effect of the intelligent PFO occluder. After 56 days of implantation, more tissue grew, and a significant increase in blood vessels appeared. After being completely covered by tissue, "endothelialization" was relatively complete to achieve autologous tissue repair. Despite changes in the material itself, the overall morphology and structural integrity of the device were maintained throughout the observation period. This indicated that the biological process of tissue ingrowth was well synchronized with the controlled degradation of the material, together ensuring long-term closure of the defect, rather than relying solely on the mechanical strength of the implant itself. This phenomenon aligned with the design rationale of biodegradable cardiovascular implants, wherein the device served as a temporary scaffold to guide tissue regeneration, with its mechanical function gradually transferred to the neotissue over time. In order to further analyze the mechanism of rapid endothelialization after implantation, the surface morphology of HUVECs was analyzed. As shown in Figure 6D, HUVECs were distributed within the tissue, exhibiting a prominent porous filamentous fibrin network and demonstrating exceptional adhesion properties, which served as an indicator of endothelialization [27, 28]. With the increase in implantation time, the number of HUVECs in tissues increased, and the coverage, density, and fiber diameter of the filamentous fibrin network increased significantly. After 56 days of implantation, the density of the porous filamentous fibrin network was higher. Compared with 0 % CLO8, the 3 % CLO8 and 4.5 % CLO8 formed a more complex network structure under the action of MV at a faster rate and with a higher density, further verifying the pro-endothelial effect of the intelligent PFO occluder.

Systematic histological analysis of the tissues surrounding the intelligent PFO occluder was performed. 14 days after implantation, a large number of inflammatory cells and a small number of newly formed blood vessels were revealed in the Hematoxylin-Eosin (H.E.) staining, with thin red lines on the inner surface of the vessels and ill-defined endothelial cells (Figure 7A) [29]. 28 days after implantation, the inflammatory response subsided, blood vessels continued to grow, degradation products appeared, and connective tissue increased. After 56 days, the fibrous tissue was dense, the neovascularization was mature, the connective tissue was directionally distributed, and the neo-endothelial tissue was clearly visible. As the concentration of the drug increased, the rate of endothelialization also accelerated significantly.

Masson staining was used for the revalidation of histological analysis. As shown in Figures 7B and S26, the collagen extracellular matrix was blue, the cytoplasm was purple, and the purplish red was the neo-vasculature. Over time, blue collagen signals progressively intensified, with scattered thin collagen deposits observed at 14 days, the collagen area significantly increased with more continuous fiber bundles at 28 days, and densely packed,

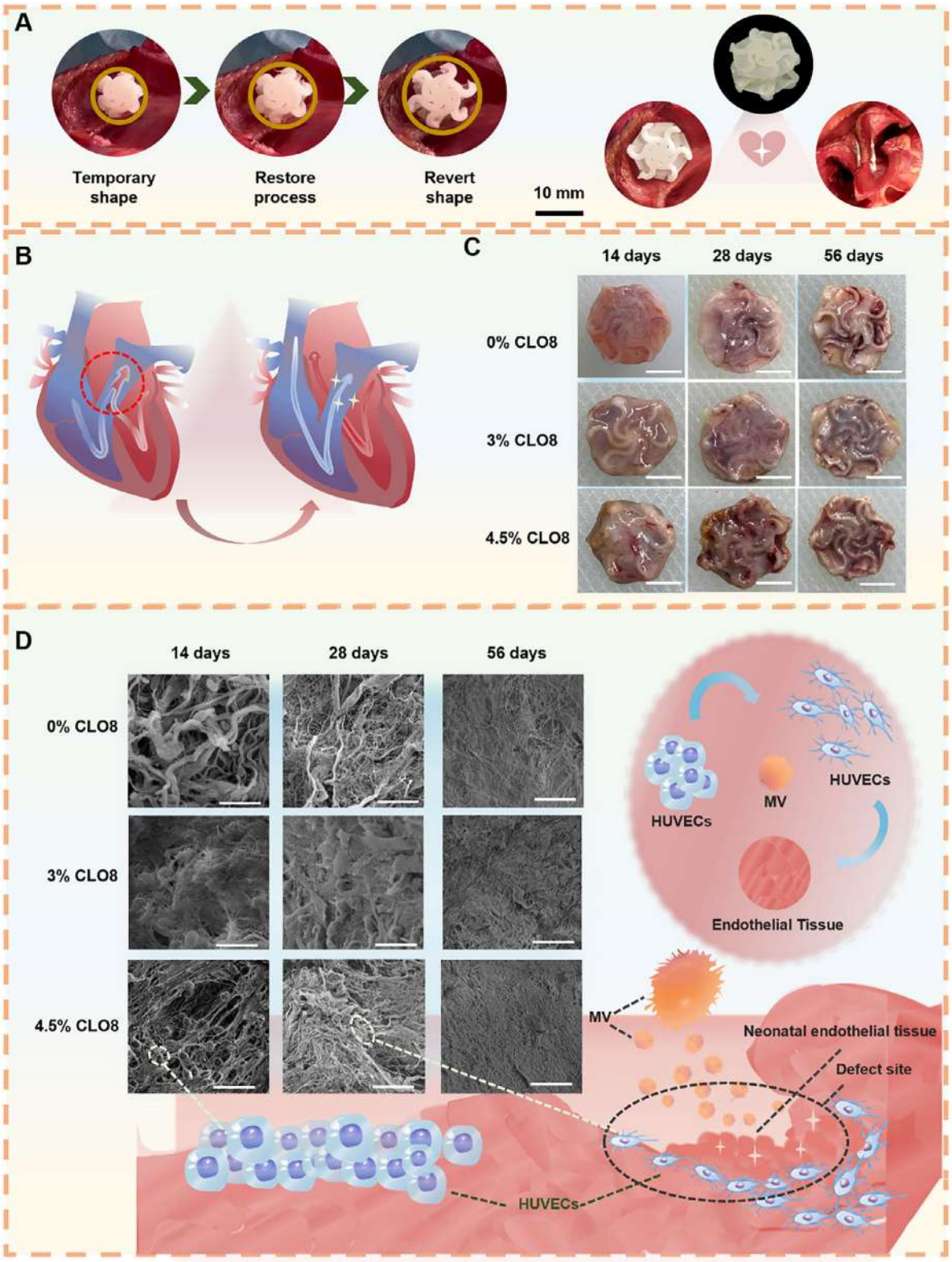

FIGURE 6 | The reconfigurable and pro-endothelial performance of the intelligent PFO occluder. (A) Physical diagram of the reconfigurable shape memory performance and occlusion effect of the intelligent PFO occluder. (B) Schematic of the repair of the intelligent PFO occluder. (C) Physical diagrams of the intelligent PFO occluder at various implantation times. Scale bar = 8 mm. (D) Morphological characterization of the endothelialization function of the intelligent PFO occluder. Scale bar = 20 μm.

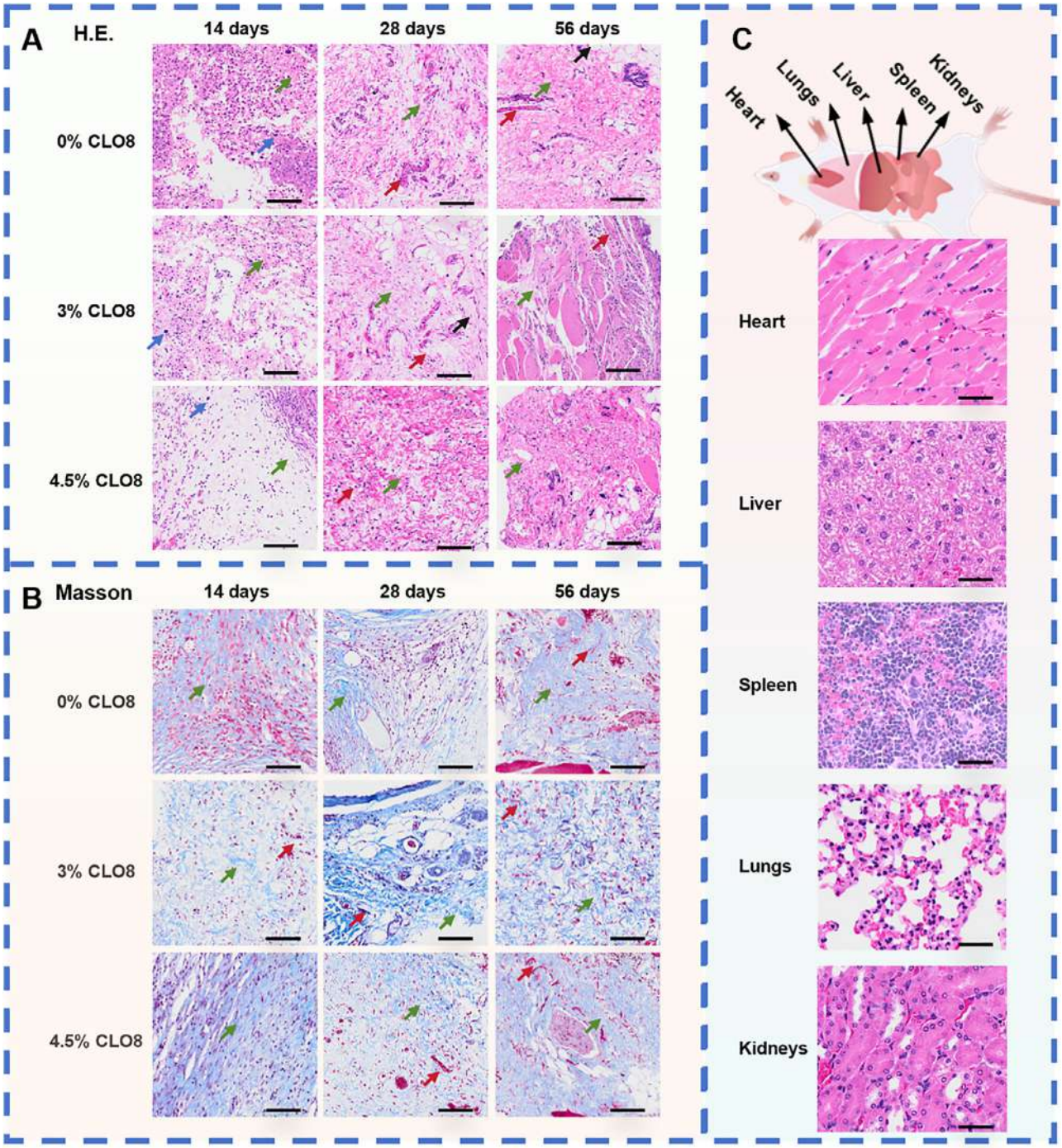

FIGURE 7 | Analysis of H.E. and Masson staining of surrounding tissues after implantation of the intelligent PFO occluder. (A) H.E staining of the intelligent PFO occluder at different drug concentrations and implantation times. Red arrows: blood vessels; Blue arrows: inflammatory cells; Green arrow: connective tissue; Black arrows: degenerated tissue. Scale bar = 50 μm. (B) Masson staining of the intelligent PFO occluder at different drug concentrations and implantation times. Red arrows: blood vessels; Green arrow: connective tissue. Scale bar = 50 μm. (C) H.E staining of major organs of rats with 4.5 % CLO8 after implantation at 56 days. Scale bar = 50 μm.

continuous, and oriented collagen matrices formed locally after 56 days. At matched time points, the 3 % and 4.5 % CLO8 groups exhibited higher collagen area ratios than the 0 % CLO8 group, for example, the collagen area of the 3 % group increased by about 1.4 times compared with the 0 % group in 28 days, and the collagen area in the 4.5 % group was about 1.5 times that of the 0 % group. In summary, Masson staining analysis further revealed that the collagen area showed a trend of accelerated collagen deposition and matrix remodeling with the increase of drug concentration. The biocompatibility was further assessed by histological analysis of major organs (Figures 7C; S27–S31). Histological analysis showed that the intelligent PFO occluder did not cause an obvious inflammatory response after implantation in the body, and showed good biocompatibility.

Immunofluorescence staining was employed to identify the expression of endothelial cell markers CD31 and VWF (Figure 8A–D). Both CD31 and VWF were stained yellow-green, and endothelial nuclei were blue. CD31 is a specific endothelial marker that reflects endothelial cell density and functional activity by mean fluorescence intensity (MFI). In the 0 % CLO8 group, MFI values were approximately 0.7 at 14 days, 1.0 at 28 days, and 1.5 at 56 days. The 3 % CLO8 group showed values of 0.8 (14 days), 1.2 (28 days), and 1.9 (56 days), while the 4.5 % CLO8 group exhibited 1.2 (14 days), 2.0 (28 days), and 2.3 (56 days). Statistically significant differences existed across time points and CLO8 concentrations. Higher intensities indicated superior endothelial coverage and endothelialization efficacy, confirming that the 4D-printed PFO occluder effectively promoted endothelial regeneration over time. The 4.5 % CLO8 group demonstrated the most substantial effect at 56 days (about 2.3), corresponding to high endothelial coverage.

VWF is a critical endothelial functional marker that indicates endothelial secretory capacity via MFI. In the 0 % CLO8 group, VWF MFI measured 0.6 (14 days), 0.9 (28 days), and 1.9 (56 days). For the 3 % CLO8 group, values were 1.0 (14 days), 1.3 (28 days), and 2.2 (56 days), while the 4.5 % CLO8 group registered 1.5 (14 days), 1.9 (28 days), and 2.6 (56 days). Significant intergroup differences were observed. Elevated VWF intensity reflected enhanced endothelial secretory function, which was crucial for maintaining vascular homeostasis and preventing thrombosis. Both time and CLO8 concentration positively regulated VWF expression, with the 4.5 % CLO8 group achieving peak intensity at 56 days (about 2.6), indicating robust endothelial activity.

In summary, CD31 and VWF expression all increased with prolonged implantation (from 14 to 56 days) and higher CLO8 concentrations (from 0 % to 4.5 %), demonstrating that the 4D-printed PFO occluder effectively promotes endothelialization and sustains endothelial function. These findings provide compelling evidence for the device's biocompatibility and potential clinical benefits in PFO therapy.

2.3.4 | Anti-Thrombosis Performance

The anti-thrombosis effect of the intelligent PFO occluder was preliminarily proved, and the physical images of the device implanted in the body were observed, with no obvious thrombus found. The plasma prothrombin time (PT), thrombin time (TT), and activated partial thromboplastin time (APTT) of 0 % CLO8 were 15.73 ± 0.24 s, 35.55 ± 3.40 s, and 41.25 ± 1.04 s, respectively. The PT, TT, and APTT times of 3 % CLO8 were 738.79 ± 36.27 s, 1272.05 ± 49.24 s, and 443.45 ± 11.66 s, respectively. PT, TT, and APTT times of 4.5 % CLO8 were 1186.71 ± 18.23 s, 1657.83 ± 65.70 s, and 591.48 ± 19.94 s, respectively (Figure 8E). It can be seen that there is an increase in DE concentration correlated with an increase in clotting time. In comparison to the 0 % CLO8 group, the clotting time was extended by more than tenfold, indicating remarkable anti-thrombosis properties. In addition, PT increased rapidly with increasing DE concentration, possibly because DE can reduce the thrombin activity of related clotting factor inhibitors, leading to a decrease in clotting factor, thereby prolonging PT.

H.E. staining results showed that thrombus complexes were observed on the 0 % CLO8, while fewer blood cells were observed on the 3 % CLO8 and 4.5 % CLO8 (Figure 8F). DE demonstrated hematological safety and potent thromboresistance, characterized by its capability to suppress platelet activation and aggregation. This translates to enhanced thrombosis prevention within the intelligent PFO occluder and a substantial lowering of thrombotic complications risk following device placement.

It should be noted that although coagulation time tests are standardized methods widely used internationally and are often used as common indicators to evaluate the hemocompatibility and antithrombotic properties of biomaterials, they cannot fully simulate the complex hemodynamic environment and platelet function in the body, which is a limitation of this study. Future research will undoubtedly progress to large animal cardiac PFO models that more closely approximate the physiological environment to comprehensively validate their hemodynamic performance and long-term sealing efficacy.

3 | Conclusion

In summary, the 4D-printed intelligent reconfigurable PFO occluder was developed, which possessed the advantages of pro-endothelial, efficient anti-thrombosis, bio-absorbability, and personalization. A series of biomimetic microstructural networks had been designed to achieve J-type stress–strain response characteristics that match the mechanical response of biological tissues, thereby helping to reduce wear and other related complications. Remarkably, the occluder demonstrated exceptional durability, maintaining structural integrity even after 1000 pressure compression cycles. Microscopic morphological analysis of in vitro degradation and in vivo histological studies confirmed the bioabsorbability of the intelligent PFO occluder, with a weight loss ratio increasing over time. The simulated occlusion experiment highlighted the excellent reconfigurability of the intelligent PFO occluder, effectively closing the PFO defect. Furthermore, the intelligent PFO occluder exhibited significant reductions in thrombin activity, providing preliminary evidence of its anti-thrombosis efficacy. Notably, the intelligent PFO occluder demonstrated encouraging outcomes in enhancing endothelialization, which was a critical step for tissue repair and remodeling. The multifunctional drug-loaded occlusion layer facilitated complete tissue encapsulation, as evidenced by immunofluorescence staining showing increased expression of CD31 and VWF markers. Therefore, a 4D-printed intelligent reconfigurable PFO occluder was highly beneficial for accelerating tissue repair and remodeling, and can be an excellent candidate for bioabsorbable, personalized, rapid endothelialization, and anti-thrombotic repair devices.

4 | Experimental Section

4.1 | Materials

Unless otherwise stated, all solvents and chemicals were acquired commercially and used as received. PLA (90 % purity), PEG (PharmPure grade), methylene chloride (99.9 % purity), barium

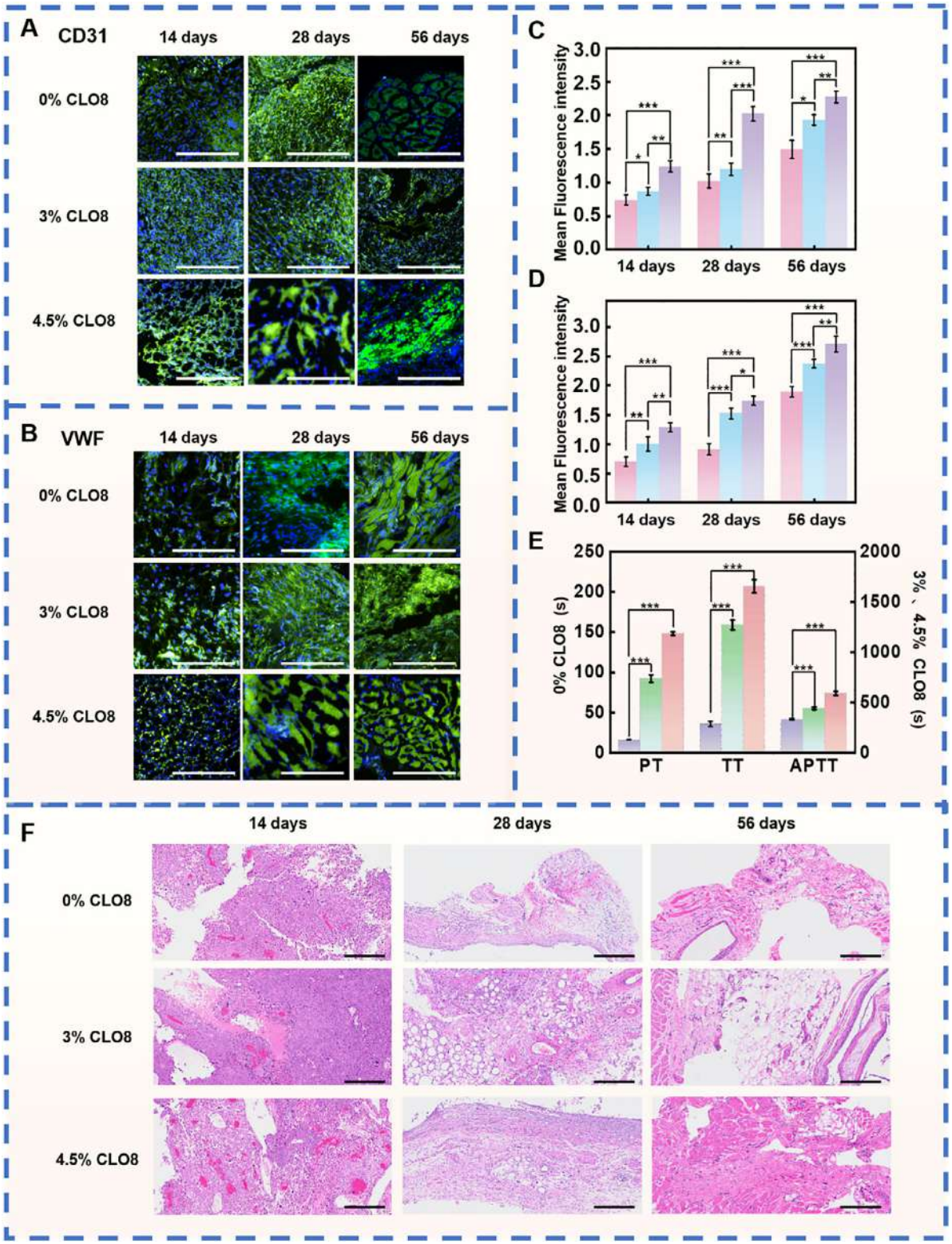

FIGURE 8 | Characterization of anti-thrombosis and endothelial function of the intelligent PFO occluder. (A,B) Expression of CD31 and VWF. (The brightness of this image was uniformly enhanced for optimal visualization. Note that all measurements and analyses were conducted using the original, unprocessed image files.) Scale bar = 300 μm. (C) The average fluorescence intensity of CD31 at 0 % CLO8, 3 % CLO8, and 4.5 % CLO8 after different implantation times (n = 3, ***$p < 0.001$, pink: 0 %CLO8, blue: 3 %CLO8, purple: 4.5 %CLO8). (D) The average fluorescence intensity of VWF at 0 % CLO8, 3 % CLO8, and 4.5 % CLO8 after different implantation times (n = 3, ***$p<0.001$, pink: 0 %CLO8, blue: 3 %CLO8, purple: 4.5 %CLO8). (E) Effect of different concentrations of PT, TT, and APTT on the intelligent PFO occluder at different concentrations and implantation times. The left coordinates are 0 % CLO8, the right coordinates are 3 % CLO8 and 4.5 % CLO8 (n = 3, ***$p < 0.001$, purple: 0 %CLO8, green: 3 %CLO8, orange: 4.5 %CLO8). (F) Distribution of thrombus of the intelligent PFO occluder at different concentrations and implantation times, with red aggregates representing blood cells. Scale bar = 400 μm.

sulfate (99.9 % purity), DE (97 % purity), MV (96 % purity), glutaraldehyde (70 % purity), and paraformaldehyde (95 % purity) were all purchased from Aladdin. H.E. staining kit was obtained from Sangon Bioengineering (Shanghai, China). PT, TT, APTT, and Masson staining were purchased from Solarbio Life Sciences (Beijing, China). CD31 polyclonal antibody and VWF polyclonal antibody were obtained from Thermo Fisher Scientific (Massachusetts, USA).

4.2 | Preparation of Multifunctional Drug-Loaded Occlusion Layer

PLA particles were used as the matrix, and PEG particles were mixed with PLA in the proportions of 10 %, 20 %, 30 % and 40 %, followed by stirring at 33°C for 3 h until fully dissolved. MV and DE were added at the ratios of 0 %, 3 %, 4.5 %, 6 %, and 7.5 %, and stirred for another 3 h to prepare the multifunctional drug-loaded occlusion layer.

4.3 | Preparation of the Intelligent Reconfigurable PFO Occluder

PLA particles and PEG particles were thoroughly mixed by a twin-screw extruder at a ratio of 2:8, and 0.2 % $BaSO_4$ was also added as a developer. Composite filaments were fabricated using a twin-screw extruder with a nozzle diameter of 1.75 mm, extrusion speed of 50 rpm, and barrel temperature of 170°C–190°C. The biomimetic microstructure network and the 4D printed shape memory framework were printed on Siemens PLM Software UG NX 1980 and printed with the composite filament on the 3D printer (TENLOG HANDS2). The 4D printed shape memory framework was combined with the multifunctional drug-loaded occlusion layer, and the 4D printed intelligent reconfigurable PFO occluder was fabricated.

4.4 | Characterization of the Multifunctional Drug-Loaded Occlusion Layer

The chemical bond characterization was performed by FTIR spectroscopy (Nicolet iS50, Thermo-Fisher Scientific). The scanning range was 4000–400 cm^{-1}. Crystal properties were analyzed using an XRD (SmartLab SE, Rigaku). The scanning speed was 5° min^{-1}, and the angle range was 5°–50°. The thermal performance was obtained by DSC (Netzsch STA 449 F5 Jupiter, Selb). The sample was heated to 180°C at a rate of 15 K min^{-1}. The microscopic morphology of the sample was observed by SEM (MIRA4, Tescan), the sample size was 5 mm × 5 mm, and the gold spraying time was 60 s. Sample tensile and compression experiments were performed using the Zwicke 010 mechanical machine. The multifunctional membrane was prepared as 10 mm × 70 mm strip samples and a test speed of 5 mm min^{-1}. In the tensile cycle test, the maximum and minimum loads for cycles were set at 1 and 3 N, respectively, and the number of cycles was set at 500. In the compression cycle test, the maximum and minimum loads for cycles were set at 1 and 2 N, respectively, and the number of cycles was set at 1000.

4.5 | Drug Release Experiment

Drug release was profiled by immersing 0.4 g of DE-MV/gPLA membranes at varying drug loading concentrations (0 %, 3 %, and 4.5 %) in 20 mL of PBS solution (pH 7.2–7.4) under light-protected conditions at 37°C. At predetermined intervals, 3 mL aliquots of supernatant were collected for UV spectrophotometric analysis of drug release rates. The formula for the cumulative release of the drug is as follows:

$$Q_n = \sum_{i=1}^{n-1} \left(C_i \times V_s \times \frac{V_{\text{total}}}{V_{r,i}} \right) + C_n \times V_{r,n}$$

where C_i is the drug concentration at the ith sampling, V_s is the sampling volume, V_{total} is the initial volume, $V_{r,\,i}$ is the remaining volume before the ith sampling, and $V_{r,\,n}$ is the remaining volume before the nth sampling.

The formula for calculating the cumulative release rate of the drug is:

$$\mathrm{R_n}\,(\%) = \frac{Q_n}{M_{total}} \times 100\,\%$$

where M_{total} is the total mass of the drug in the drug loading matrix, Q_n is the cumulative release of the drug.

4.6 | In Vitro Degradation Experiments

The samples were submerged in phosphate-buffered saline (PBS, pH 7.2–7.4) and incubated at 37°C incubator to evaluate the degradation behavior. The sample was removed at a preset time, followed by washing and drying until the weight of the sample remained unchanged. The bioabsorbability of the sample was assessed by regularly testing the weight loss.

4.7 | Reconfigurable Shape Memory Performance

The porcine heart represents the most widely used analog for the human heart in experimental cardiology, exhibiting high similarity in atrial septal thickness, atrial chamber dimensions, and hemodynamics. A 5 mm tunnel-like PFO-mimetic defect was surgically created in the right atrial septum of the in vitro porcine heart to replicate the clinical PFO anatomy. The sample was placed in a heated temperature chamber so that it rose from room temperature to the conversion temperature above the conversion temperature, and then the temperature was maintained for 5 min. The external force was applied to the sealer to produce the desired temporary configuration; the external force was kept constant, and the cooling setting was quickly removed for 5 min. The occluder was delivered via a 10F catheter to the defect site and subsequently activated by thermal stimulus to achieve shape recovery. When the temperature of the sample was raised again above the transition temperature, the sample automatically returned to its permanent configuration, exhibiting reconfigurable properties. The specific formula for calculating the

recovery rate of shape memory is as follows:

$$R_r\,(\%) = \frac{L_t - L_1}{L_t - L_0} \times 100$$

where L_t was the length of the temporary shape disk, L_1 was the length after shape memory stimulation, and L_0 was the length of the initial shape.

4.8 | Verification of Occluding Function

The PFO model was established in a fresh pig heart using needles for puncture, and the intelligent PFO occluder was programmed to a temporary configuration of small volume. The intelligent PFO occluder in the temporary configuration was transported to the PFO and automatically returned to the permanent configuration under thermal stimulation.

4.9 | In Vivo Histocompatibility Analysis

The animal experiments were approved by the Ethics Committee of the First Affiliated Hospital of Harbin Medical University (2023113). Given the ethical complexities, resource requirements, and technical challenges associated with large animal heart model experiments, the Sprague–Dawley (SD) rats were chosen. The intelligent PFO occluder was implanted into sterilized male rats using SD rats for in vivo histocompatibility evaluation. The core biological processes of artificially constructed defects and physiological PFO repair in this process are highly similar, including endothelial migration, collagen deposition, and angiogenesis. SD rats are widely used in the evaluation of cardiovascular devices. By analyzing the effects of occluder implantation on endothelial migration, collagen deposition, angioproliferation, etc., during the defect repair process, the validation of the defect repair function of the occluder can be effectively reflected, so as to evaluate the curative effect of PFO. SD rats were sacrificed at 14 days, 28 days, and 56 days postoperatively, and the intelligent PFO occluder and adjacent tissues were collected at each time point. The important organs and the intelligent PFO occluder wrapped in the new intima were removed and fixed with paraformaldehyde for 2 days. Tissue sections were stained with H.E. and observed under light microscopy. The intelligent PFO occluder was fixed with 5 % glutaraldehyde overnight, washed with 0.9 % ice saline, gradient dehydrated, and dried in a 4°C freezer. One part was observed by SEM, and the other part was frozen for mason staining. SEM and staining were used to evaluate the relationship between the degree of endothelialization and implantation time and drug concentration.

4.10 | In Vivo Immunofluorescence Staining

SD rats were sacrificed at 14, 28, and 56 days after surgery, and sectioned after fixation, gradient dehydration, and embedding. After washing and freezing, add primary antibodies and incubate overnight. The next day, the fluorescent secondary antibody was washed and incubated at 37°C for 2 h, and the microscopic morphology of the samples was detected with confocal fluorescence microscopy.

4.11 | Anti-Thrombosis Tests

The multi-functional drug-loaded occlusion layer was prepared and fixed on a 24-well culture plate. The diluted 2 mL of rat whole blood was incubated with the layer at 37°C for 1 h, and 200 μL of platelet-free plasma was collected. The adhesion of platelets was evaluated using a scanning electron microscope. Activated partial thromboplastin, prothrombin, and thrombin were used to determine APTT, PT, and TT values.

4.12 | Statistical Analysis

Each experiment was repeated at least three times. Quantitative results are expressed as mean ± standard deviation. Student's t-test was used to compare groups, and significance was marked as $^{*}p < 0.05$, $^{**}p < 0.01$, $^{***}p < 0.001$, and $^{****}p < 0.0001$.

Author Contributions

Jinsong Leng, Yanju Liu, Liwu Liu, and Cheng Lin conceived the concept. Jingfei Wang wrote the paper. Cheng Lin and Jingfei Wang designed the experiments. Jingfei Wang conducted the materials and mechanics experiments. Fukai Liu, Shuting Li, and Jingfei Wang conducted the biological experiments. All authors discussed the results.

Acknowledgements

The work was supported by the Key R&D Program of Ningbo City (No.2023Z191), the open research fund of Suzhou Laboratory (No. SZLAB - 1508 - 2024ZD016), the State Key Laboratory of Mechanics and Control for Aerospace Structure (Nanjing University of Aeronautics and astronautics) (No. MCAS - E - 0125K01) and the Open Project of National Key Laboratory of Aerospace Mechanism (No. 2024ASM - KF03).

Conflicts of Interest

The authors declare no competing interests.

Data Availability Statement

The data that support the findings of this study are available from the corresponding author upon reasonable request.

References

1. C. K. Skibsted, K. Pedersen, L. Bonnesen, K. Nielsen-Kudsk, and M. Schmidt, "Long-Term Risk of Atrial Fibrillation or Flutter After Transcatheter Patent Foramen Ovale Closure: A Nationwide Danish Study," *European Heart Journal* 44 (2023): 3469–3477, https://doi.org/10.1093/eurheartj/ehad305.

2. C. Yan and H. Li, "Preliminary Investigation of in Situ Thrombus Within Patent Foramen Ovale in Patients With and Without Stroke," *Jama* 325 (2021): 2116–2118, https://doi.org/10.1001/jama.2021.4359.

3. B. O. Grory, E. Feng, et al., "Advances in the Management of Cardioembolic Stroke Associated With Patent Foramen Ovale," *Bmj* 376 (2022): e063161, https://doi.org/10.1136/bmj-2020-063161.

4. M. H. Alkhouli, H. Yao, and D. Holmes, "Effectiveness of Transcatheter Closure of Patent Foramen Ovale in Clinical Practice," *Journal of the American Heart Association* 12 (2023): 030321, https://doi.org/10.1161/JAHA.123.030321.

5. M. Dupuy, P. Guedeney, J. Silvain, et al., "Feasibility and Early Outcomes of Atrial Septal Defect Prostheses Use for Percutaneous Closure

of Widely Open Patent Foramen Ovale," *European Heart Journal* 45 (2024): hae6662478, https://doi.org/10.1093/eurheartj/ehae666.2478.

6. P. Guedeney, M. Laredo, M. Zeitouni, et al., "Supraventricular Arrhythmia Following Patent Foramen Ovale Percutaneous Closure," *JACC: Cardiovascular Interventions* 15 (2022): 2315–2322, https://doi.org/10.1016/j.jcin.2022.07.044.

7. Z. Xiang, J. Zhang, C. Zhou, et al., "Near-Infrared Remotely Controllable Shape Memory Biodegradable Occluder Based on Poly(l -lactide-co -ε-caprolactone)/Gold Nanorod Composite," *ACS Applied Materials & Interfaces* 15 (2023): 42341–42353, https://doi.org/10.1021/acsami.3c09852.

8. Z. Li, P. Kong, X. Liu, et al., "A Fully Biodegradable Polydioxanone Occluder for Ventricle Septal Defect Closure," *Bioactive Materials* 24 (2023): 252–262, https://doi.org/10.1016/j.bioactmat.2022.12.018.

9. C. Lin, J. Lv, Y. Li, et al., "4D-Printed Biodegradable and Remotely Controllable Shape Memory Occlusion Devices," *Advanced Functional Materials* 29 (2019): 1906569, https://doi.org/10.1002/adfm.201906569.

10. Y. Zhang, J. Wang, J. Xiao, et al., "An Electrospun Fiber-Covered Stent With Programmable Dual Drug Release for Endothelialization Acceleration and Lumen Stenosis Prevention," *Acta Biomaterialia* 94 (2019): 295–305, https://doi.org/10.1016/j.actbio.2019.06.008.

11. C. Lin, M. Yang, F. Zhang, Y. Liu, and J. Leng, "Stimuli-Responsive Smart Materials For Biomedical Applications," *Materials Science and Engineering: R: Reports* 167 (2026): 101126, https://doi.org/10.1016/j.mser.2025.101126.

12. D. Yan, J. Chang, H. Zhang, et al., "Soft Three-Dimensional Network Materials With Rational Bio-Mimetic Designs," *Nature Communications* 11 (2020): 1180, https://doi.org/10.1038/s41467-020-14996-5.

13. X. P. Li, W. Wu, W. Xiong, and Y. Lu, "Auxetic Mechanical Metamaterials: From Soft to Stiff," *International Journal of Extreme Manufacturing* 5 (2023): 042003, https://doi.org/10.1088/2631-7990/ace668.

14. M. Tannu, R. D. Lopes, D. M. Wojdyla, et al., "Antithrombotic Therapy to Minimize Total Events After ACS or PCI in Atrial Fibrillation," *Journal of the American College of Cardiology* 85 (2025): 1157–1168, https://doi.org/10.1016/j.jacc.2024.10.125.

15. C. Liu, M. Shen, W. L. W. Tan, et al., "Statins Improve Endothelial Function via Suppression of Epigenetic-Driven EndMT," *Nature Cardiovascular Research* 2 (2023): 467–485, https://doi.org/10.1038/s44161-023-00267-1.

16. S. Dehnavi, A. Kiani, M. Sadeghi, et al., "Targeting AMPK by Statins: A Potential Therapeutic Approach," *Drugs* 81 (2021): 923–933, https://doi.org/10.1007/s40265-021-01510-4.

17. C. L. Lin, L. Liu, and J. Leng, "Recent Developments in Next-Generation Occlusion Devices," *Acta Biomaterialia* 128 (2021): 100–119, https://doi.org/10.1016/j.actbio.2021.04.050.

18. Z. M. Meng, X. He, J. Zhang, J. Ling, and D. Li, "Embedding Aligned Nanofibrous Architectures Within 3D-Printed Polycaprolactone Scaffolds for Directed Cellular Infiltration and Tissue Regeneration," *International Journal of Extreme Manufacturing* 5 (2023): 025001, https://doi.org/10.1088/2631-7990/acbd6c.

19. S. I. Senaysoy and H. Lekesiz, "Mechanical Deviation in 3D-Printed PLA Bone Scaffolds During Biodegradation," *Computers in Biology and Medicine* 183 (2024): 109227, https://doi.org/10.1016/j.compbiomed.2024.109227.

20. A. R. Monfared, H. Omranpour, A. V. Tuccitto, et al., "Sustainable PLA Bio-Nanocomposites: Integration of TPU Nanofibrils and CNC for Enhanced Crystallization, Toughness, Stiffness, Transparency, and Oxygen Barrier Properties," *ACS Sustainable Chemistry & Engineering* 12 (2024): 13017–13029, https://doi.org/10.1021/acssuschemeng.4c05231.

21. L. H. Ge, X. Zhang, et al., "A Dabigatran Etexilate Phospholipid Complex Nanoemulsion System for Further Oral Bioavailability by Reducing Drug-Leakage in the Gastrointestinal Tract," *Nanomedicine* 14 (2017): 1455–1464, https://doi.org/10.1016/j.nano.2017.08.009.

22. C. Shuai, Z. Wang, H. Zhang, et al., "Biosoluble Ceramic Fiber Reinforced Poly (L-Lactic Acid) Bone Scaffold: Degradation and Bioactivity," *NPJ Materials Degradation* 6 (2022): 87, https://doi.org/10.1038/s41529-022-00297-3.

23. X. X. Wan and Z. Tian, et al., "Recent Advances in 4D Printing of Advanced Materials and Structures for Functional Applications," *Advanced Materials* 36, no. 34 (2024): 2312263, https://doi.org/10.1002/adma.202312263.

24. X. L. Xin, L. Liu, and J. Leng, "4D Printing Auxetic Metamaterials With Tunable, Programmable, and Reconfigurable Mechanical Properties," *Advanced Functional Materials* 30, no. 43 (2020): 2004226, https://doi.org/10.1002/adfm.202004226.

25. J. Y. Liu and Y. Zhang, "Mechanics of Unusual Soft Network Materials With Rotatable Structural Nodes," *Journal of the Mechanics and Physics of Solids* 146 (2021): 104210, https://doi.org/10.1016/j.jmps.2020.104210.

26. E. Z. Zappino, N. Petrolo, M. Vaziri, R. Carrera, and A. Poursartip, "Analysis of Process-Induced Deformations and Residual Stresses in Curved Composite Parts Considering Transverse Shear Stress and Thickness Stretching," *Composite Structures* 241 (2020): 112057, https://doi.org/10.1016/j.compstruct.2020.112057.

27. P. Y. Yu, F. Li, et al., "HUVECS′ Expressway Based on Magnesium Ion Doped Hierarchical Scaffold for Rapid Angiogenesis and Bone Ingrowth," *Advanced Functional Materials* 35 (2024): 2417614, https://doi.org/10.1002/adfm.202417614.

28. X.-W. Wang, Y.-J. Yin, J. Wang, et al., "UV-Triggered Hydrogel Coating of the Double Network Polyelectrolytes for Enhanced Endothelialization," *Advanced Science* 11 (2024): 2401301, https://doi.org/10.1002/advs.202401301.

29. W. Wang, X. Li, X. Ding, et al., "Lymphatic Endothelial Transcription Factor Tbx1 Promotes an Immunosuppressive Microenvironment to Facilitate Post-Myocardial Infarction Repair," *Immunity* 56 (2023): 2342–2357.e10, https://doi.org/10.1016/j.immuni.2023.07.019.

Supporting Information

Additional supporting information can be found online in the Supporting Information section.

Supporting File: adhm70884-sup-0001-SuppMat.docx